Supplementary Material

V. Dzanic[1], C. S. From[2]† and E. Sauret[1]‡

[1]School of Mechanical, Medical, and Process Engineering, Faculty of Engineering, Queensland University of Technology, QLD 4001, Australia

[2]Department of Chemical Engineering, University of Manchester, Manchester M13 9PL, UK

(Received xx; revised xx; accepted xx)

This supplementary material consists of additional results and simulations using the Oldroyd-B model at different levels of periodicity and grid resolution. More specifically, figures 1 and 2 correspond to figures 2 and 3 in the main text. Here, the additional figures show the vorticity and polymer fields for the full-size domain for the R16, R36, and R64 cases.

Figures 3 and 4 show the results for an additional simulation conducted using periodicity with $n = 8$, corresponding to 256 rollers, referred to as R256. Figure 3 illustrates that the qualitative properties of the flow overcome the effects of a single-leading vortex, partly retaining the effects of the initial four-roll mill forcing structure even at very high levels of periodicity, further supporting the results in the main text. Figure 4 reveals that the chaotic dynamics of the system are also adhered to for the R256 case, thus confirming that the R64 case is a sufficiently high-level of periodicity to assess and compare the dynamics of the problem in the main text.

Finally, figures 5 and 6 illustrate results for the R4 case at a refined grid resolution of 256^2. Figure 5 shows analogous results to the vorticity and polymer field contours obtained in the main text using a grid resolution of $(n \times N)^2 = (n \times 128)^2$ [refer to figures 2 (a) and 3 (a)]. The quasi-periodic dynamics observed in the polymer field is also obtained at the refined grid resolution (figure 6), supporting that the observed periodic dynamics are induced from a lack of periodicity as opposed to insufficient grid resolution. We also tested the grid-dependence of a case pertaining to higher levels of periodicity $n \gtrsim 1$. More specifically, we ran the R36 case ($n = 3$) at a refined grid resolution of $(n \times N)^2 = 768^2$, showing that the vorticity and polymer fields are still slaved to the background forcing symmetry (figure 7). When observing the time-series of C_{xx} in figure 8, it is clear that solutions agree well in the steady-state region $0 \leqslant t/T \leqslant 400$. Although different results are observed for the refined solution at the onset of the chaotic regime $t/T \gtrsim 400$, we note that these differences are attributed to the late-time chaos of the simulation. Overall, the large-scale dynamics of the refined R36 solution undergo the main features of the chaotic results presented in the main text for $n \gtrsim 1$ (i.e. flow symmetry and chaotic dynamics).

† Email address for correspondence: christopher.from@manchester.ac.uk
‡ Email address for correspondence: emilie.sauret@qut.edu.au

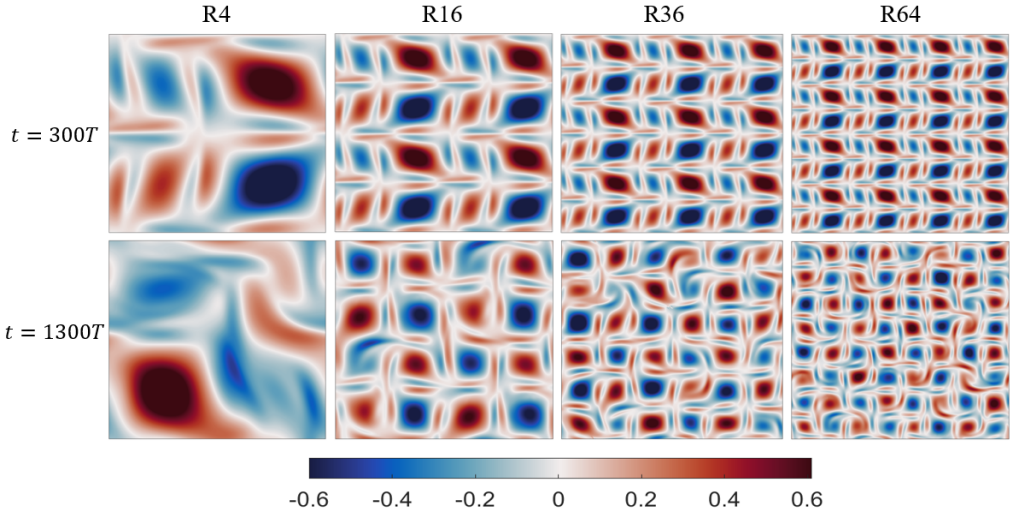

FIGURE 1. Contour plots of the vorticity field for the full-size domain for each case, from left to right: R4, R16, R36, and R64 at $Wi = 10$ (top row) during the initial symmetry breaking $t = 300T$ and (bottom row) within the elastic turbulence regime $t = 1300T$.

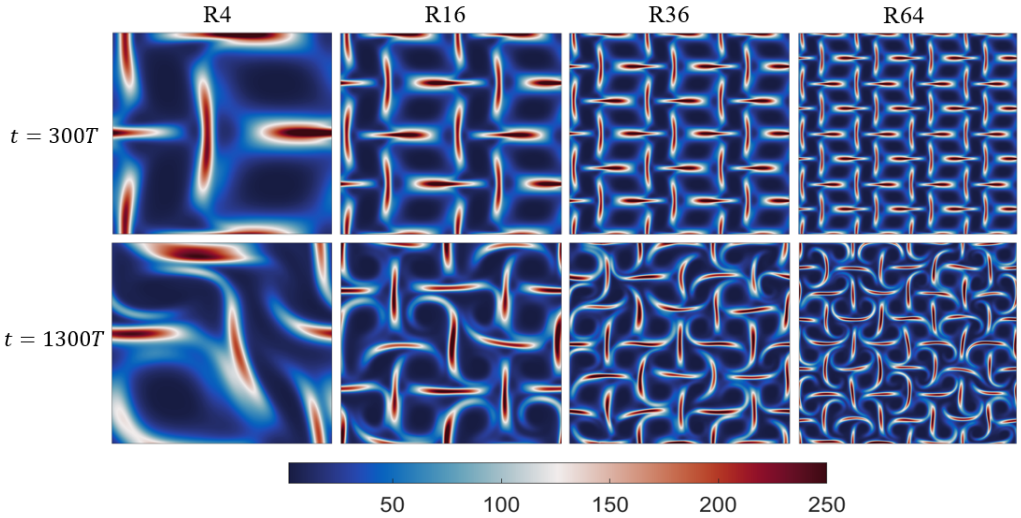

FIGURE 2. Contour plots of the conformation tensor trace tr($\boldsymbol{C}$) for the full-size domain for each case, from left to right: R4, R16, R36, and R64 at $Wi = 10$ (top row) during the initial symmetry breaking $t = 300T$ and (bottom row) within the elastic turbulence regime $t = 1300T$.

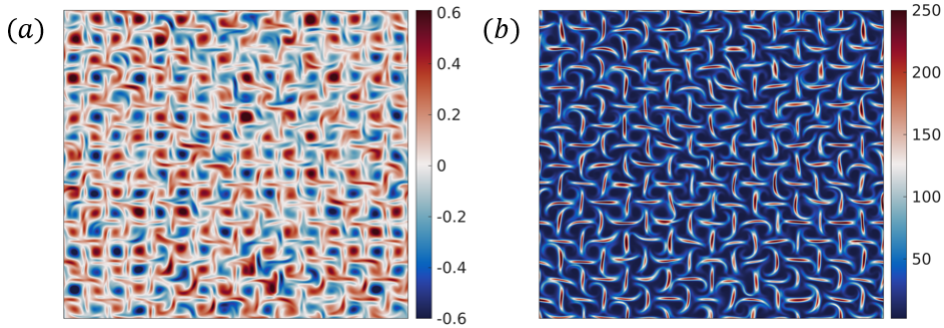

FIGURE 3. Contour plots for (a) the vorticity field and (b) the conformation tensor trace tr($\boldsymbol{C}$) taken at the late stages corresponding to $t = 1300T$ for the R256 case (n=8) at $Wi = 10$.

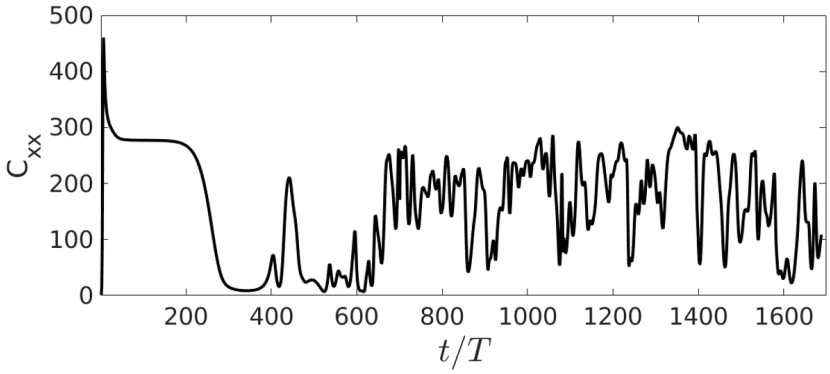

FIGURE 4. Time series $0 \leqslant t/T \leqslant 1700$ of the first component of the conformation tensor C_{xx} at the position $[\pi, \pi]$ for the R256 case (n=8) at $Wi = 10$.

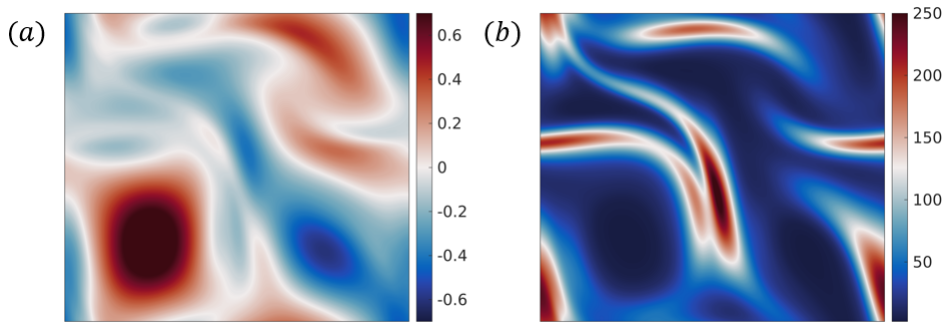

FIGURE 5. Contour plots for (a) the vorticity field and (b) the conformation tensor trace tr($\boldsymbol{C}$) taken at the late stages corresponding to $t = 1300T$ for the R4 case at $Wi = 10$ using a refined grid resolution of $(n \times N)^2 = 256^2$.

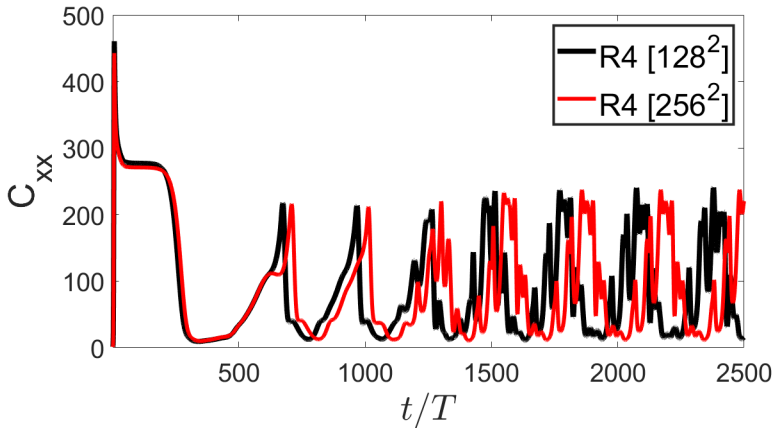

FIGURE 6. Time series $0 \leqslant t/T \leqslant 2500$ of the first component of the conformation tensor C_{xx} at the position $[\pi, \pi]$ for the R4 case at $Wi = 10$ using grid resolutions of $N^2 = 128^2$ (black) and $N^2 = 256^2$ (red). Note, results at 128^2 are the same as reported in main text.

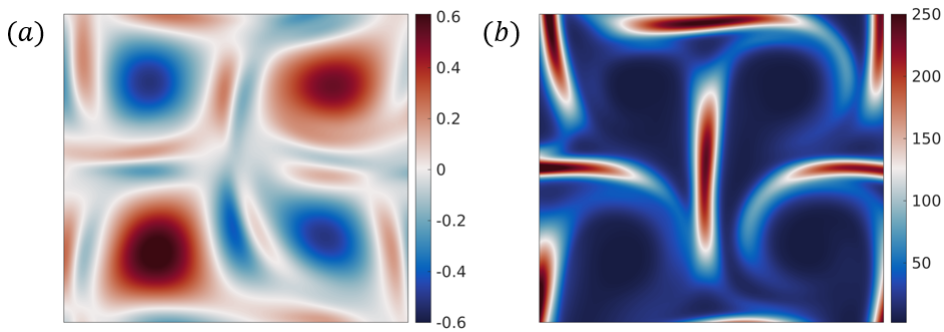

FIGURE 7. Contour plots for (a) the vorticity field and (b) the conformation tensor trace tr($\boldsymbol{C}$) taken at the late stages corresponding to $t = 1300T$ for the R36 case ($n = 3$) at $Wi = 10$ using a refined grid resolution of $(n \times N)^2 = 768^2$.

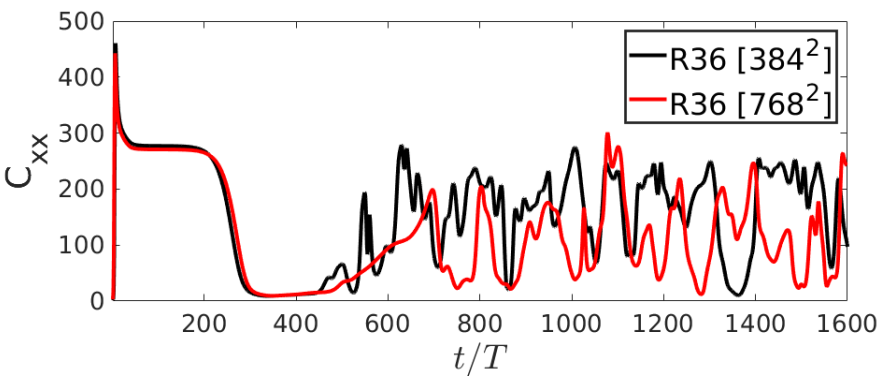

FIGURE 8. Time series $0 \leqslant t/T \leqslant 1600$ of the first component of the conformation tensor C_{xx} at the position $[\pi, \pi]$ for the R36 case ($n = 3$) at $Wi = 10$ using grid resolutions of $(n \times N)^2 = 384^2$ (black) and $(n \times N)^2 = 768^2$ (red). Note, results at 384^2 are the same as reported in main text.